AIAA JOURNAL
Vol. 49, No. 4, April 2011

Conceptual Design of Compliant Mechanisms for Flapping Wings with Topology Optimization

Bret Stanford* and Philip Beran†
U.S. Air Force Research Laboratory, Wright-Patterson Air Force Base, Ohio 45433

DOI: 10.2514/1.J050940

This work discusses the integration of two previously disparate research areas: topology optimization of compliant mechanisms and flapping wing vehicles. The efficient actuation of the latter is considerably challenging, with competing weight, energy, and authority requirements; intuitive design strategies are not typically available for the aeroelastic physics that define the flapping system. We discuss the incorporation of these physics into a gradient-based topological optimization scheme, to design thrust-optimal compliant flapping mechanisms. This is done with a nonlinear dynamical finite element model incorporating both the mechanism and the wing structure, coupling elastic, inertial, aerodynamic, and actuator forces. Several optimal mechanism topologies are presented, along with a detailed discussion of the relevant flapping physics driving the design process.

Nomenclature

$a_{x'}$, $a_{z'}$	=	wing acceleration
$\boldsymbol{B}$	=	strain-displacement matrix
c	=	wing chord
$\boldsymbol{C}_e$, $\boldsymbol{C}$, $\boldsymbol{C}^*$	=	elemental, global, and Jacobian damping matrices
C_L, C_T, C_P	=	lift, thrust, and power coefficients
C_{xz}, C_D, C_R	=	force and rotation coefficients
$dF_{x'}$, $dF_{z'}$, $d\tau_{y'}$	=	sectional forces and torque
$dF^v_{x'}$, $dF^v_{z'}$, $dM^v_{y'}$	=	viscous forces and moment
$\boldsymbol{E}$	=	plane stress constitutive matrix
f	=	actuation force
$\boldsymbol{F}_{\text{aero}}$	=	aerodynamic force vector
$\boldsymbol{F}_{\text{in}}$	=	actuation force vector
g, G	=	average and instantaneous optimization metrics
$\boldsymbol{G}$	=	vector of terms from the previous time step
grey*	=	intermediate density constraint
H_{radius}	=	gradient filter radius
k	=	reduced frequency ($\omega \cdot c/2/U_\infty$)
k_o, k_e	=	baseline and element support spring stiffness
$\boldsymbol{K}_s$, $\boldsymbol{K}^*$	=	support stiffness and Jacobian stiffness matrices
l, l_e	=	wing and element lengths
$\boldsymbol{M}_e$, $\boldsymbol{M}$, $\boldsymbol{M}^*$	=	elemental, global, and Jacobian mass matrices
N_e, N_{steps}	=	number of mechanism elements and time steps
$\boldsymbol{P}$	=	internal elastic force vector
P	=	input power
p_k, p_z, p_m, p_c	=	penalization factors
$\boldsymbol{R}$	=	residual vector
Re	=	Reynold's number ($\rho_f \cdot U_\infty \cdot c/\mu$)
R_{tol}	=	convergence omission threshold
$\boldsymbol{s}^T$, S, S^*	=	support constraint terms
$\boldsymbol{s}_e$	=	elemental Piola–Kirchhoff stress
T	=	flapping time period
$\boldsymbol{T}$	=	sectional-global transformation matrix
t	=	time
t_o, t_f	=	time steps used to bound optimization metric
U_∞	=	flow velocity
$\boldsymbol{u}_e$, $\boldsymbol{u}$	=	elemental and global displacement vectors
$\dot{\boldsymbol{u}}$, $\ddot{\boldsymbol{u}}$	=	global velocity and acceleration vectors
u^{in}, u^*	=	input displacement constraint terms
$\boldsymbol{v}^T$, V, V^*	=	volume constraint terms
$v_{x'}$, $v_{z'}$	=	wing velocity
x, y, z	=	global coordinate system
x', y', z'	=	local coordinate system
x_e, $\boldsymbol{x}$, $x_{\min}$	=	elemental, global, and lower bound relative densities
z_e, $\boldsymbol{z}$, $z_{\min}$	=	elemental, global, and lower bound support variables
α	=	angle of attack
α_o	=	damping coefficient
α_s	=	sectional angle of attack
β, γ	=	Newmark integration parameters
Γ	=	circulation
$\boldsymbol{\varepsilon}_e$	=	elemental Green-Lagrange strain
$\lambda_{x'}$, $\lambda_{z'}$, I_a	=	added mass terms
μ	=	viscosity
μ_1, μ_2	=	dimensionless viscous parameters
ρ_f	=	fluid density
σ_{mech}, σ_{wing}	=	mechanism and wing von Mises stress
$\dot{\psi}$, $\ddot{\psi}$	=	axial wing rotational velocity and acceleration
ω	=	actuation frequency

Presented as Paper 2010-9095 at the AIAA Multidisciplinary Analysis and Optimization Conference, Fort Worth, TX, 13–15 September 2010; received 16 September 2010; revision received 22 December 2010; accepted for publication 27 December 2010.

*National Research Council Postdoctoral Researcher; bret.stanford@wpafb.af.mil.

†Principal Research Aerospace Engineer; philip.beran@wpafb.af.mil.

I. Introduction

DESIGN and optimization for flapping wing flyers is a research area that is still largely in its infancy, though has received a great deal of attention in recent years: see review articles by Ho et al. [1] and Shyy et al. [2,3]. Standard aeronautical design practices have little relevancy for flapping wings of course, where the flight physics are dominated by nonlinear, unsteady, aeroelastic, and viscous mechanisms. It is expected that all of these areas will need to be exploited for the development of an agile, stable, and efficient flapping wing, though intuitive ideas as to how this can be done are not readily available in most cases. As such, conceptual design with numerical optimization should play a substantial role in vehicle development. A review of the existing literature reveals design studies (Isogai and Harino [4], Berman and Wang [5], Soueid et al. [6], Stanford and Beran [7], and Stanford et al. [8]) that incorporate wing structure, wing shape, and/or kinematic motion design

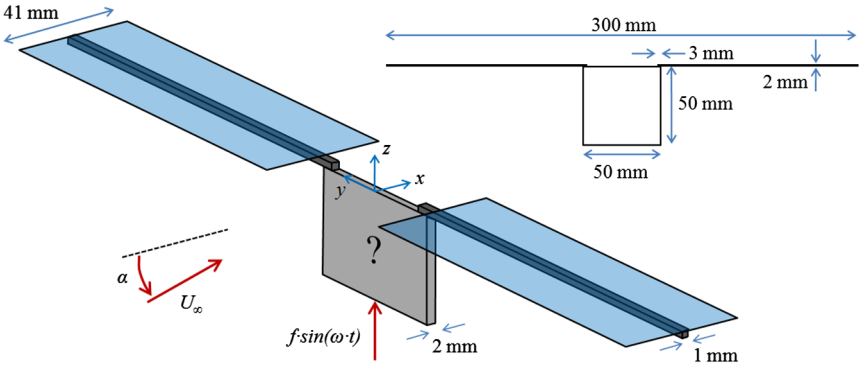

Fig. 1 Actuated flapping wing in forward flight.

variables. While a great deal of insight can certainly be obtained from such studies, the details of the actuation mechanisms themselves are usually considered to be known, fixed quantities. Particularly when dealing with kinematic design, such an assumption can be extremely erroneous [9].

Experimentally, mechanism design has proven to be one of the most challenging aspects of flapping wing flyer development [10,11]. The mechanism must be able to provide an adequate range of wing motion at a suitable frequency for both lift and thrust generation, its power consumption is limited to what is available onboard, and the mass of the mechanism itself should not be more that what is available from the aerodynamic forces. Many mechanisms are constructed that appear to meet these goals, only to have the operable flapping frequency drop drastically when a wing is attached to the mechanism.[‡] As such, it would seem necessary to develop an optimization framework that simultaneously considers mechanism and wing design, as the details of each are inherently linked. The current work is focused largely on mechanism optimization, but structure and shape variables pertaining to the wing design (see Maute and Allen [12] and Stanford and Ifju [13] for work concerning topology design of aeroelastic fixed wings) could be included into the framework.

It has been speculated that compliant mechanisms may be superior to the multijointed variety for miniature actuation, in terms of assembly, tolerance, and friction [14]; and are biologically inspired as well (an insect's thorax, e.g., [15]). The prudent placement of springs within four-bar linkage drive mechanisms for flapping wings is shown by Madangopal et al. [16] and Tantanawat and Kota [17] to be successful in minimizing the input power requirements. The latter research effort also provides a detailed overview on the relevant flow of energy between the aerodynamic, elastic, inertial, and input forces of a compliant flapping mechanism, and how this flow can be tailored for efficient actuation.

Topology optimization for compliant mechanisms (where a design space is discretized into elements, each element can be solid or void, and the objective might be to maximize the ratio of the output to the input displacement) is a well-established tool: see Sigmund [18] and Bendsøe and Sigmund [19] for a general overview. Geometrically nonlinear behavior has long been realized as a necessary inclusion for topology optimization of mechanisms [20,21], but transient structural dynamic applications [22,23] and aeroelastic applications [24] are very rare. The method, to the best of the authors' knowledge, has never been used for flapping mechanisms. Outfitting the topology optimization problem with prudent constraints and objectives may lead to a flapping mechanism that satisfies many of the basic requirements given above, without any substantial assumptions made about its shape or operability a priori. In a more general sense, the research presented below discusses a problem where nonlinear dynamics and coupled fluid-structure interactions drive the design process, factors which, to the authors' knowledge, have also never been included in a single framework for topology optimization.

[‡]Personal communication with D. Doman [2010].

This work considers the topological design of a two-dimensional compliant mechanism with a sinusoidal input actuation force (whose origin is unspecified) connected to a flexible wing capable of motions within a two-dimensional plane. The wing and mechanism dynamics are coupled, computed with a single unified finite element model. The structural composition of the wing is fixed for this work, focusing for now on the optimal topology of the compliant mechanism. Aerodynamic loads are applied to the flexible wing, computed with a quasi-steady blade element model. These loads are complex nonlinear functions of the wing deformation, complicating both the system response computations and the required design gradients.

II. Problem Definition

The general problem definition is illustrated in Fig. 1. The mechanism is constrained to fit within a two-dimensional square, subjected to a sinusoidal vertical point load at the bottom. This bounding box is 5 cm on each side, 2 mm thick, and constructed of an acrylonitrile butadiene styrene (ABS) plastic, a material widely used in rapid-prototyping machines, and found to be useful for the construction of flapping wings as well [25]. The rectangular wings are sealed to a flexible rod along the half-chord location; the rod is in turn connected to the upper corners of the mechanism box. Each rod is 12.5 cm long with a rectangular cross section (2 by 1 mm), and constructed of bidirectional plain-weave carbon fiber. The length of each wing is the same as its rod, and the chord is 4.1 cm. These overall dimensions are summarized in Fig. 1; the material properties used for structural modeling are given in Table 1. As will be discussed below, the rectangular wing is not explicitly modeled in the structural analysis (instead a massless entity prescribed to rigidly follow the flexible rod motions), and so the wing material is unspecified, and its properties are not given in Table 1.

The actuation eventually provided by the compliant mechanism will produce simple flapping motions in the y-z plane. The entire vehicle is subjected to a freestream velocity U_∞, inclined to the x-axis by an angle of attack α. If the compliant mechanism is able to overcome the aerodynamic loading applied to the wing and the inertial loading of both the wing and the mechanisms itself, the flapping angle of the wings (and thus the Strouhal number) will be sufficiently large to produce a propulsive thrusting force in the $-x$ direction [26], overcoming the drag of the wings and vehicle body. As summarized in Table 2, the resulting Reynolds number ($Re = \rho_f \cdot U_\infty \cdot c/\mu$) is 27,750 and the reduced frequency ($k = \omega \cdot c/2/U_\infty$) is 0.205.

A schematic of the two-dimensional finite element model is given in Fig. 2. Only half of the setup in Fig. 1 is considered, using a symmetry-plane at the z-axis, and the lower corner of the mechanism box is constrained from moving in either direction (fixed to the wing body). Both the mechanism and the wing rod are idealized with a single finite element model, discretized into square Q4 elements [27]. The aerodynamic forces are only applied to nodes that lie along the lower surface of the wing. Only the external aerodynamic forces normal to the mesh seen in Fig. 2 (i.e., those forces that lie in the y-z plane) are used; axial forces and pitching moments are available from the aerodynamic tool, but cannot be applied to the mesh in light of the

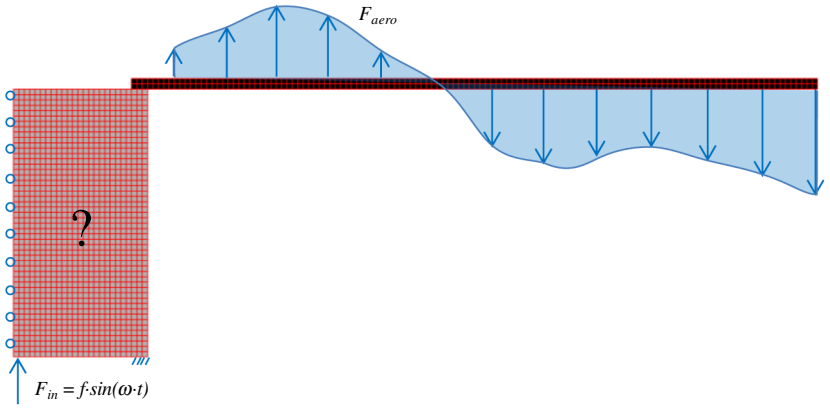

Fig. 2 Finite element model of both the mechanism and the wing.

two-dimensional assumption. These additional forces and moments can be used, however, to quantitatively assess the force production, efficiency, and stability of the flapping wing. In keeping with these assumptions, the rectangular wing is assumed to be perfectly rigid in both a chordwise and torsional sense, though spanwise bending is obviously permitted.

The topology optimization problem considered here follows the standard procedure [19]. Each of the bilinear finite elements within the mechanism region in Fig. 2 is assigned a design variable, its relative density. This density should be either zero (void) or unity (solid). The optimal distribution of material should ideally be binary (i.e., all 0's or 1's), but during the optimization procedure intermediate values are permitted with an interpolation function governing the material properties between the two extremes. Intermediate densities are then penalized during the optimization, either implicitly or explicitly, to provide the desired binary distribution.

It should be explicitly noted that only the topology of the mechanism is designed during the optimization; the structural composition of the finite elements within the wing are held fixed. It is also desired to design the underlying support structure of the mechanism (in addition to the clamped boundary condition in the lower corner of Fig. 2). This is done with the method of Buhl [28], where each finite element within the mechanism region is assigned a second design variable: the stiffness of 8 springs attached to each of the four nodes. It is desired that this stiffness be either too small to affect the system, or large enough that the element can be considered clamped. As above, intermediate values are permitted with an interpolation function bridging the two extremes.

III. Mechanism Modeling

The dynamic behavior of the finite element model shown in Fig. 2 is governed by a balance of elastic, inertial, aerodynamic, and actuator forces at each time step. The sections given below formulate each of these components individually, followed by a unified aeroelastic model.

A. Elastic Forces

Geometrically nonlinear behavior must be included in the topological design of a mechanism which will use slender structures undergoing large elastic deformations [20,21]. The variation of the Green–Lagrange strain pseudovector within each Q4 element is written as [27]:

$$\delta \boldsymbol{\varepsilon}_e = \boldsymbol{B}(\boldsymbol{u}_e) \cdot \delta \boldsymbol{u}_e \tag{1}$$

where $\boldsymbol{u}_e$ is a vector of elemental nodal displacements, and $\boldsymbol{B}$ is a nonlinear strain-displacement matrix. The Piola–Kirchhoff stress pseudovector within each element is given by:

$$\boldsymbol{s}_e = (x_e)^{p_k} \cdot \boldsymbol{E} \cdot \boldsymbol{\varepsilon}_e \tag{2}$$

where $\boldsymbol{E}$ is the constitutive matrix for plane stress of the solid isotropic material, x_e is the relative density of each element (ranging from a small nonzero value to unity), and p_k is the stiffness-based penalization factor [20]. The nonlinear internal force vector for the entire finite element system is finally given as an assembly over each finite element e, consisting of both the mechanism and wing elements:

$$\begin{aligned} \boldsymbol{P}(\boldsymbol{u}) &= \sum_e \left(\int (\boldsymbol{B}^T(\boldsymbol{u}_e) \cdot \boldsymbol{s}_e) \cdot \mathrm{d}V_e \right) \\ &= \sum_e \left((x_e)^{p_k} \cdot \int (\boldsymbol{B}^T(\boldsymbol{u}_e) \cdot \boldsymbol{E} \cdot \boldsymbol{\varepsilon}_e) \cdot \mathrm{d}V_e \right) \end{aligned} \tag{3}$$

where $\boldsymbol{u}$ is a vector of global nodal displacements of the entire finite element system. The formulation of the tangent stiffness matrix associated with Eq. (3) ($\partial \boldsymbol{P}/\partial \boldsymbol{u}$), is given as a sum of the linear, material, and geometric stress stiffness terms; a derivation can be found in [27].

It should be noted that the assembly of Eq. (3) (and similar operations discussed below) loops over each finite element in Fig. 2, both the mechanism's and the wing's. The x_e quantities in the wing structure are fixed at 1, and correspond to the material properties for carbon fiber (Table 1; used to build $\boldsymbol{E}$). The x_e quantities in the mechanism are allowed to vary during the optimization process, and correspond to the material properties for acrylonitrile butadiene styrene plastic.

As discussed above, it is also desired to design the underlying support structure of the mechanism. Following the methodology of Buhl [28], eight springs are attached to the nodes of each bilinear element within the mechanism, seen in Fig. 3. It should be noted that the springs do not connect two elements; one end of the spring is fixed in space (rigid), the other is connected to a Q4 element's node, and each Q4 element is connected to a distinct set of eight springs (four oriented horizontally, four vertically). For a given Q4 element, the stiffness of each of the attached eight springs is identical, and given by:

$$k_e = (z_e)^{p_z} \cdot k_o \tag{4}$$

where z_e is a second design variable associated with each mechanism Q4 finite element, ranging from a small nonzero value to unity, and

Table 1 Structural parameters for the mechanism and the wing rod

	Mechanism	Wing rod
Material	ABS plastic	Carbon fiber
Elastic modulus	2 GPa	40 GPa
Poisson's ratio	0.3	0.3
Density	1000 kg/m^3	1400 kg/m^3
Thickness	2 mm	1 mm
Failure stress	35 MPa (yield)	80 MPa (matrix cracking)
Damping, α_o	5	5

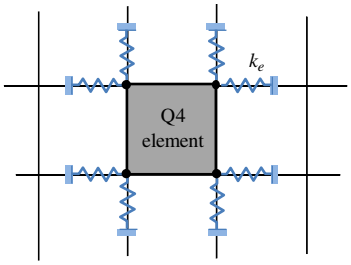

Fig. 3 Eight support springs connecting the nodes of each bilinear finite element to the ground.

p_z is a support penalization factor. The baseline spring stiffness k_o is sized to an appropriately large value such that, when z_e is unity the bilinear element can be considered fixed. When z_e is equal to $z_{\min}$, the springs should provide a negligible stiffness to the complete finite element system. $z_{\min}$ is larger than zero, however, such that spring supports that are forced to the lower bound have the ability to reappear during the optimization process [19]. The support stiffness matrix of the entire finite element system is then assembled as:

$$\boldsymbol{K}_s = \sum_e ((z_e)^{p_z} \cdot \text{diag}\{k_o, k_o, k_o, k_o, k_o, k_o, k_o, k_o\}) \tag{5}$$

B. Inertial Forces

Similarly, a consistent global mass and damping matrix can be found from the following assemblies:

$$\boldsymbol{M} = \sum_e (\boldsymbol{M}_e \cdot (x_e)^{p_m}) \qquad \boldsymbol{C} = \sum_e (\boldsymbol{C}_e \cdot (x_e)^{p_c}) \tag{6}$$

where $\boldsymbol{M}_e$ and $\boldsymbol{C}_e$ are the elemental mass and damping matrices of the solid material, and p_m and p_c are mass- and damping-based penalization factors. Rayleigh damping is used for the current work:

$$\boldsymbol{C}_e = \alpha_0 \cdot \boldsymbol{M}_e \tag{7}$$

The proportionality factor is given in Table 1. A similar stiffness-proportional damping term is not included due to well-known accuracy issues encountered with such a term in nonlinear structural dynamics [29], found to be problematic here as well. It can be seen that the assembled $\boldsymbol{C}$ is not necessarily proportional to $\boldsymbol{M}$ if the associated penalization factors differ.

C. Aerodynamic Forces

A quasi-steady two-dimensional blade element model is used to compute the aerodynamic forces and moments over the flapping wing. As seen in Fig. 4, a coordinate system (x'-y'-z') is attached to the center of each wing section as it goes through the flapping motion. A transformation matrix between the local system and the global system (x-y-z) seen in Fig. 1 can be computed for each section from the solution $\boldsymbol{u}$. The three sectional quantities seen in Fig. 4 are computed using expressions given below [Eqs. (8–10), with spanwise forces assumed to be zero], and then the terms are integrated over each Q4 element along the lower surface of the wing mesh. The forces and moments are transformed back into the x-y-z frame, and then the forces that lie in the y-z plane are used to populate $\boldsymbol{F}_{\text{aero}}$. Additional information pertaining to the integration of blade element aerodynamics into an aeroelastic framework is found in [8].

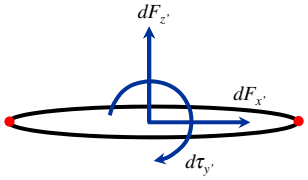

Fig. 4 Wing section and coordinate system used for aerodynamic modeling.

The blade element model is taken from the work of Berman and Wang [5], and will be briefly summarized here. The sectional forces and torque on a wing section during the flapping cycle are:

$$dF_{x'} = (\lambda_{z'} \cdot v_{z'} \cdot \dot{\psi} - \rho_f \cdot \Gamma \cdot v_{z'} - \lambda_{x'} \cdot a_{x'}) \cdot dy' - dF^v_{x'} \tag{8}$$

$$dF_{z'} = (-\lambda_{x'} \cdot v_{x'} \cdot \dot{\psi} + \rho_f \cdot \Gamma \cdot v_{x'} - \lambda_{z'} \cdot a_{z'}) \cdot dy' - dF^v_{z'} \tag{9}$$

$$d\tau_{y'} = ((\lambda_{z'} - \lambda_{x'}) \cdot v_{x'} \cdot v_{z'} + I_a \cdot \ddot{\psi}) \cdot dy' - dM^v_{y'} \tag{10}$$

where ρ_f is the density of the fluid, and $v_{x'}$, $v_{z'}$, $a_{x'}$, and $a_{z'}$ are the velocity and acceleration of the wing (computed with $\dot{\boldsymbol{u}}$ and $\ddot{\boldsymbol{u}}$), written in the wing coordinate system. Similarly, $\dot{\psi}$ and $\ddot{\psi}$ are the axial rotational velocity and acceleration of the wing about the y' axis. $\lambda_{x'}$, $\lambda_{z'}$, and I_a are added mass terms, and Γ is the circulation:

$$\Gamma = -0.5 \cdot C_{xz} \cdot c \cdot \sqrt{v^2_{x'} + v^2_{z'}} \cdot \sin(2 \cdot \alpha_s) + 0.5 \cdot C_R \cdot c^2 \cdot \dot{\psi} \tag{11}$$

where C_{xz} and C_R are the translational and rotational force coefficients, α_s is the wing section's angle of attack, and c is the local chord length. The viscous terms given above are computed by:

$$\begin{Bmatrix} dF^v_{x'} \\ dF^v_{z'} \end{Bmatrix} = 0.5 \cdot \rho_f \cdot c \cdot (C_D(0) \cdot \cos^2(\alpha_s) + C_D(\pi/2) \cdot \sin^2(\alpha_s)) \cdot \sqrt{v^2_{x'} + v^2_{z'}} \cdot \begin{Bmatrix} v_{x'} \\ v_{z'} \end{Bmatrix} \cdot dy' \tag{12}$$

$$dM^v_{y'} = \frac{1}{16} \cdot \pi \cdot \rho_f \cdot c^4 \cdot (\mu_1 \cdot \omega/(2 \cdot \pi) + \mu_2 \cdot |\dot{\psi}|) \cdot \dot{\psi} \tag{13}$$

where C_D is the drag coefficient, μ_1 and μ_2 are dimensionless viscous parameters, and ω is the flapping frequency.

Many of the terms used above will be zero for the current study (specifically those related to rotation about the y' axis), but are included for completeness. The parameters used to define Eqs. (8–13) are given in Table 3, where the derivation of the added mass terms is provided in [5]. The final aerodynamic force is:

$$\boldsymbol{F}_{\text{aero}} = \sum_e \boldsymbol{T}(\boldsymbol{u}_e) \cdot l_e \cdot \{ dF_{x'} \quad dF_{z'} \quad d\tau_{y'} \}^T \tag{14}$$

where the assembly in Eq. (14) only occurs over the bilinear elements along the lower surface of the wing mesh; no aerodynamic force is assumed to act within the compliant mechanism, and l_e is the length of the element. The three sectional quantities of Eqs. (8–10) need to be transformed into elemental force vectors which can be applied to the finite element system. This is done via the 8×3 matrix $\boldsymbol{T}(\boldsymbol{u}_e)$, which first distributes the sectional forces/torques acting along the

Table 2 Forward flight flapping parameters

Parameter	Value	Parameter	Value
Chord, c	4.1 cm	Angle of attack, α	0°
Wing length, l	12.5 cm	Actuation force, f	15 N
Flow velocity, U_∞	10 m/s	Frequency, ω	100 rad/s (15.91 Hz)

Table 3 Quasi-Steady aerodynamic parameters

Parameter	Value	Parameter	Value
ρ_f	1.225 kg/m^3	μ_1	0.2
C_{xz}	π	μ_2	0.2
$C_D(0)$	0.04	$\lambda_{x'}$	0 kg/m
$C_D(\pi/2)$	2	$\lambda_{z'}$	$1.671 \cdot 10^{-3}$ kg/m
C_R	π	I_a	$9.062 \cdot 10^{-8}$ kg · m

lower surface of the element $\{\, dF_{x'} \quad dF_{z'} \quad d\tau_{y'} \,\}$ to the two lower nodes of the bilinear element in an energy-equivalent manner. Secondly, it transforms the quantities from the body-attached x'-y'-z' system to the global x-y-z system using standard coordinate-transformation techniques. Third, it strips out all terms except the forces that lie in the y-z plane, as the two-dimensional model used here (Fig. 2) will not respond to moments or out-of-plane forces. Finally, $\boldsymbol{T}(\boldsymbol{u}_e)$ places zeros into the degrees of freedom associated with the two upper nodes.

D. Aeroelastic Solver

Using Eqs. (3), (5), (6), and (14), the final equations of motion for the unsteady deformations of the mechanism and the wing are:

$$\boldsymbol{M}\cdot\ddot{\boldsymbol{u}} + \boldsymbol{C}\cdot\dot{\boldsymbol{u}} + \boldsymbol{P}(\boldsymbol{u}) + \boldsymbol{K}_s\cdot\boldsymbol{u} = \boldsymbol{F}_{\text{aero}}(\boldsymbol{u},\dot{\boldsymbol{u}},\ddot{\boldsymbol{u}}) + \boldsymbol{F}_{\text{in}}(t) \tag{15}$$

where $\boldsymbol{F}_{\text{in}}$ is the oscillating point load seen in Fig. 2. The aerodynamic force vector is generally a nonlinear function of the wing displacement and its time-derivatives, and is zero at degrees of freedom pertaining to mechanism motion, as discussed above.

Equation (15) is solved via an implicit time marching scheme, with Newton–Raphson subiterations within each time step to drive the nonlinear residual below a specified tolerance. At the $n+1$ time step, this residual is:

$$\begin{aligned}\boldsymbol{R}_{n+1} \equiv{}& \left(\frac{1}{\beta\cdot\Delta t^2}\cdot\boldsymbol{M} + \frac{\gamma}{\beta\cdot\Delta t}\cdot\boldsymbol{C} + \boldsymbol{K}_s\right)\cdot\boldsymbol{u}_{n+1} + \boldsymbol{P}_{n+1} + \boldsymbol{G}_n \\ &- \boldsymbol{F}_{\text{aero}}(\boldsymbol{u}_{n+1},\dot{\boldsymbol{u}}_{n+1},\ddot{\boldsymbol{u}}_{n+1}) - \boldsymbol{F}_{\text{in}}(t_{n+1}) = \boldsymbol{0}\end{aligned} \tag{16}$$

where γ and β are standard Newmark integration parameters, and $\boldsymbol{G}_n$ are terms known from the previous time step:

$$\begin{aligned}\boldsymbol{G}_n = {}& \boldsymbol{M}\cdot\left(\frac{1}{\beta\cdot\Delta t^2}\cdot(-\boldsymbol{u}_n - \Delta t\cdot\dot{\boldsymbol{u}}_n) - \frac{1}{2\cdot\beta}\cdot\ddot{\boldsymbol{u}}_n\right) \\ &+ \boldsymbol{C}\cdot\left(\frac{-\gamma}{\beta\cdot\Delta t}\cdot\boldsymbol{u}_n - \left(\frac{\gamma}{\beta}-1\right)\cdot\dot{\boldsymbol{u}}_n - \Delta t\cdot\left(\frac{\gamma}{2\cdot\beta}-1\right)\cdot\ddot{\boldsymbol{u}}_n\right)\end{aligned} \tag{17}$$

This residual is driven below a specified tolerance with a standard Newton–Raphson updating procedure to compute $\boldsymbol{u}_{n+1}$. Then the time step counter is incremented by one. The Jacobian, computed analytically, is given by:

$$\frac{\partial\boldsymbol{R}}{\partial\boldsymbol{u}} = \frac{1}{\beta\cdot\Delta t^2}\cdot\boldsymbol{M}^* + \frac{\gamma}{\beta\cdot\Delta t}\cdot\boldsymbol{C}^* + \boldsymbol{K}^* \tag{18}$$

where

$$\begin{aligned}\boldsymbol{M}^* = \boldsymbol{M} - \frac{\partial\boldsymbol{F}_{\text{aero}}}{\partial\ddot{\boldsymbol{u}}} \qquad \boldsymbol{C}^* = \boldsymbol{C} - \frac{\partial\boldsymbol{F}_{\text{aero}}}{\partial\boldsymbol{u}} \\ \boldsymbol{K}^* = \frac{\partial\boldsymbol{P}}{\partial\boldsymbol{u}} + \boldsymbol{K}_s - \frac{\partial\boldsymbol{F}_{\text{aero}}}{\partial\boldsymbol{u}}\end{aligned} \tag{19}$$

IV. Optimization Details

A. Design Derivatives

The vectors of design variables $\boldsymbol{x}$ (the relative density of each finite element) and $\boldsymbol{z}$ (the support structure of each finite element) are expected to be very large, particularly if fine meshes are desired to describe the compliant mechanism. The gradients must then be computed analytically, typically with an adjoint method, which provides a computational cost nearly independent of the number of design variables [30]. Adjoint methods, however, are very cumbersome for nonlinear transient time-marching problems [31]. The differential equation for the adjoint vector is provided with a set of terminal conditions which must be integrated in reverse [32]. This then requires that the solution vector (and its time derivatives) must be stored in memory during the forward integration for the system response [Eq. (15)] at each time step. During the reverse integration, these vectors are recalled and used to construct the Jacobian [Eq. (18)] at each time step [33].

Conversely, the direct method for analytical gradients entails a differential equation with multiple right-hand sides (one per design variable) that can be integrated forward in time, along with the system response. The system response does not need to be stored in memory, and the Jacobian needed for the sensitivities will be known from the system response computation at each time step. Furthermore, the Jacobian is fairly sparse and well-banded; a large number of right-hand sides is not expected to be cumbersome [34]. For the problem described above, the direct method should be less expensive than the adjoint method, and will be used here.

It is desired to compute the derivative of a few scalar quantities (one objective function, as well as some constraints) of the aeroelastic motion with respect to $\boldsymbol{x}$ and $\boldsymbol{z}$. Each of these scalars takes the form:

$$g = \int_{t_0}^{t_f} G(\boldsymbol{u},\dot{\boldsymbol{u}},\ddot{\boldsymbol{u}},\boldsymbol{x},\boldsymbol{z})\cdot\mathrm{d}t \tag{20}$$

The function could be aerodynamic or structural in nature, and is measured over a time period between t_o and t_f. In the event that a cycle-averaged quantity is desired, $t_f = t_o + 2\cdot\pi/\omega$; for instantaneous quantities (peak thrust, for example), t_o and t_f coalesce to the same time step.

The derivative of this function with respect to $\boldsymbol{x}$ is given by:

$$\frac{\mathrm{d}g}{\mathrm{d}\boldsymbol{x}} = \int_{t_0}^{t_f}\left(\frac{\partial G}{\partial\boldsymbol{x}} + \frac{\partial G}{\partial\boldsymbol{u}}\cdot\frac{\partial\boldsymbol{u}}{\partial\boldsymbol{x}} + \frac{\partial G}{\partial\dot{\boldsymbol{u}}}\cdot\frac{\partial\dot{\boldsymbol{u}}}{\partial\boldsymbol{x}} + \frac{\partial G}{\partial\ddot{\boldsymbol{u}}}\cdot\frac{\partial\ddot{\boldsymbol{u}}}{\partial\boldsymbol{x}}\right)\cdot\mathrm{d}t \tag{21}$$

Likewise, the derivative of the aeroelastic equations of motion is:

$$\begin{aligned}&\frac{\partial\boldsymbol{M}}{\partial\boldsymbol{x}}\cdot\ddot{\boldsymbol{u}} + \boldsymbol{M}\cdot\frac{\partial\ddot{\boldsymbol{u}}}{\partial\boldsymbol{x}} + \frac{\partial\boldsymbol{C}}{\partial\boldsymbol{x}}\cdot\dot{\boldsymbol{u}} + \boldsymbol{C}\cdot\frac{\partial\dot{\boldsymbol{u}}}{\partial\boldsymbol{x}} + \frac{\partial\boldsymbol{P}}{\partial\boldsymbol{x}} + \frac{\partial\boldsymbol{P}}{\partial\boldsymbol{u}}\cdot\frac{\partial\boldsymbol{u}}{\partial\boldsymbol{x}} + \boldsymbol{K}_s\cdot\frac{\partial\boldsymbol{u}}{\partial\boldsymbol{x}} \\ &\quad= \frac{\partial\boldsymbol{F}_{\text{aero}}}{\partial\ddot{\boldsymbol{u}}}\cdot\frac{\partial\ddot{\boldsymbol{u}}}{\partial\boldsymbol{x}} + \frac{\partial\boldsymbol{F}_{\text{aero}}}{\partial\dot{\boldsymbol{u}}}\cdot\frac{\partial\dot{\boldsymbol{u}}}{\partial\boldsymbol{x}} + \frac{\partial\boldsymbol{F}_{\text{aero}}}{\partial\boldsymbol{u}}\cdot\frac{\partial\boldsymbol{u}}{\partial\boldsymbol{x}}\end{aligned} \tag{22}$$

Using the expressions given in Eq. (19), this equation is rewritten as:

$$\boldsymbol{M}^*\cdot\frac{\partial\ddot{\boldsymbol{u}}}{\partial\boldsymbol{x}} + \boldsymbol{C}^*\cdot\frac{\partial\dot{\boldsymbol{u}}}{\partial\boldsymbol{x}} + \boldsymbol{K}^*\cdot\frac{\partial\boldsymbol{u}}{\partial\boldsymbol{x}} = -\frac{\partial\boldsymbol{M}}{\partial\boldsymbol{x}}\cdot\ddot{\boldsymbol{u}} - \frac{\partial\boldsymbol{C}}{\partial\boldsymbol{x}}\cdot\dot{\boldsymbol{u}} - \frac{\partial\boldsymbol{P}}{\partial\boldsymbol{x}} \tag{23}$$

At a given time step, the matrices $\boldsymbol{M}^*$, $\boldsymbol{C}^*$, and $\boldsymbol{K}^*$ will be known from the solution of Eq. (16). Each term on the right-hand side of Eq. (23) is a known explicit derivative. Each of these terms is easily computed by analytically differentiating Eqs. (3) and (6). For example, $\partial\boldsymbol{M}/\partial x_e$ is very sparse, as only the degrees of freedom associated with the eth finite element are nonzero, and equal to $\boldsymbol{M}_e\cdot p_m\cdot(x_e)^{p_m-1}$. This sparse matrix is multiplied by $\ddot{\boldsymbol{u}}$, and the resulting vector becomes the eth column of $(\partial\boldsymbol{M}/\partial\boldsymbol{x})\cdot\ddot{\boldsymbol{u}}$. As noted then, the differential equation for $\partial\boldsymbol{u}/\partial\boldsymbol{x}$ is linear ($\boldsymbol{M}^*$, $\boldsymbol{C}^*$, and $\boldsymbol{K}^*$ are not functions of $\partial\boldsymbol{u}/\partial\boldsymbol{x}$) with time-dependent coefficients and multiple right-hand sides (the size of $\boldsymbol{x}$). This equation can be solved concurrently with the differential equation for the aeroelastic system response, forward in time [34]. The relevant terms can then be inserted into Eq. (17) to compute the sought-after design derivative $\mathrm{d}g/\mathrm{d}\boldsymbol{x}$.

A similar sensitivity analysis equation can be written for the support design variables, only with a different right-hand side:

$$\boldsymbol{M}^*\cdot\frac{\partial\ddot{\boldsymbol{u}}}{\partial\boldsymbol{z}} + \boldsymbol{C}^*\cdot\frac{\partial\dot{\boldsymbol{u}}}{\partial\boldsymbol{z}} + \boldsymbol{K}^*\cdot\frac{\partial\boldsymbol{u}}{\partial\boldsymbol{z}} = -\frac{\partial\boldsymbol{K}_s}{\partial\boldsymbol{z}}\cdot\boldsymbol{u} \tag{24}$$

This equation can be integrated in time along with Eqs. (15) and (23), and the appropriate terms inserted into a derivative function similar to Eq. (21), only written for $\boldsymbol{z}$.

B. Topology Optimization

The method of moving asymptotes [35] (MMA) is used to solve the constrained topology optimization problem:

$$\max_{x,z} g = C_{T,\text{ave}} \quad \text{s.t.:} \begin{cases} 0 < x_{\min} < x_e < 1 & e = 1, \ldots, N_e \\ 0 < z_{\min} < z_e < 1 & e = 1, \ldots, N_e \\ V(\boldsymbol{x}) = \boldsymbol{v}^T \cdot \boldsymbol{x} \leq V^* & \\ S(\boldsymbol{z}) = \boldsymbol{s}^T \cdot \boldsymbol{z} \leq S^* & \\ |u_n^{\text{in}}| \leq u^* & n = 1, \ldots, N_{\text{steps}} \\ \boldsymbol{x}^T \cdot (1 - \boldsymbol{x}) \leq \text{grey}^* & \end{cases} \tag{25}$$

where it is desired to maximize the cycle-averaged thrust coefficient. The relative density of each finite element is constrained to lie between a small nonzero value (to prevent singularities, and also allow element voids to reappear during the design process [19]) and unity. The support variables are similarly bounded.

The volume of the mechanism's design domain $V(\boldsymbol{x})$ should be below some specified value; this constraint, along with the nonlinear power-law interpolation of the mass, damping, and stiffness [Eqs. (3) and (6)] should implicitly push the design variables $\boldsymbol{x}$ to a 0–1 distribution, as intermediate values are less economical. The power-law values used here, shown in Table 4, are adopted from [23] (see the discussion therein for a rationale behind these choices for topology optimization of dynamic structures). A similar technique is applied for support design via S^* and p_z. It is further required that the magnitude of the displacement at the input point load u^{in} is less than some specified tolerance u^* at each time step, to stabilize the optimization process and provide a suitable load path between the input and output [19] (wing motion).

The final constraint of Eq. (25) is an explicit penalty upon intermediate element densities: $\boldsymbol{x}^T \cdot (1 - \boldsymbol{x})$. This constraint is added to the design problem once the implicitly penalized topology has converged (a difference less than 10^{-4} of the computed objective function g between two successive iterations). As has been noted for problems governed by unsteady [23] or coupled [24] physics, the implicit penalty upon intermediate densities may have limited effectiveness. The explicit penalty (via a suitably low value of grey*) can be used to force the design to a 0–1 distribution without substantially altering the topology of the structure.

As is typical of topology optimization problems, the design gradients $\mathrm{d}g/\mathrm{d}\boldsymbol{x}$ and $\mathrm{d}u^{\text{in}}/\mathrm{d}\boldsymbol{x}$ are subjected to a spatial filter over the design domain, to limit the minimum size of the design elements, as well as prevent checkerboard patterns. The radius of this filter H_{radius} is noted in Table 4, where a unit radius is equal to the length of each bilinear finite element. Another well-known problem that arises during topology optimization with geometric nonlinearities, and observed here as well, is the nonconvergence of the aeroelastic residual $\boldsymbol{R}_n$ at certain time steps due to oscillations of the void elements ($x_{\min}$). This problem is circumvented by removing the solution at nodes surrounded by finite elements with a density less than R_{tol} from the convergence criterion, as discussed by Pederson et al. [20].

Table 4 Topology optimization parameters

Parameter	Value	Parameter	Value	Parameter	Value
$x_{\min}$	$1 \cdot 10^{-4}$	$z_{\min}$	$1 \cdot 10^{-4}$	p_k	3
V^*	0.17–0.3	S^*	20	p_m	1
u^*	0.5–2 mm	k_o	$1 \cdot 10^8$	p_c	0.5
R_{tol}	0.05	p_z	3	H_{radius}	1.2

Using initial design vectors of $\boldsymbol{x} = V^*$, $\boldsymbol{z} = S^*$ (spatially uniform topology and support structure), an algorithmic outline of the process used to solve Eq. (25) is as follows:

1) The equations of motion [Eq. (15)] are integrated to compute the evolution of $\boldsymbol{u}$ as a function of time. Concurrently, the linear direct sensitivity equations [Eqs. (23) and (24)] are integrated to compute $\partial \boldsymbol{u}/\partial \boldsymbol{x}$ at each time step. This is done until the aeroelastic response settles into a time-periodic response, N_{steps}.

2) The thrust coefficient is a known function of u [Eq. (20)]; the objective function ($C_{T,\text{ave}}$) is computed by averaging this thrust coefficient over the final time periodic flapping cycle. The sensitivities of this objective can further be computed from $\partial \boldsymbol{u}/\partial \boldsymbol{x}$.

3) The time step at which the input displacement $|u^{\text{in}}|$ is maximum is identified. The sensitivities of this displacement are found by extracting the degree of freedom associated with u^{in} from $\partial \boldsymbol{u}/\partial \boldsymbol{x}$, at the critical time step. All the information needed to enforce the fifth constraint of Eq. (25) is then available.

4) The derivatives of the average thrust and the peak input displacement are filtered over the design domain.

5) The constraints that are independent of the aeroelastic response $\boldsymbol{u}$ are computed: $V(\boldsymbol{x})$, $S(\boldsymbol{z})$, $\boldsymbol{x}^T \cdot (1 - \boldsymbol{x})$. The sensitivities of these functions are easily obtained as well.

6) The objective function and constraints, their sensitivities, and the current design variables are provided to the MMA algorithm [35]. The algorithm returns the next design iteration ($\boldsymbol{x}$, $\boldsymbol{z}$), at which point the process returns to step 1.

The aeroelastic solver, the subsequent formulation of the problem objective function and constraints, and the MMA algorithm are all implemented in the MATLAB programming language.

V. Results

All results are computed on the 25×50 grid seen in Fig. 2, with 50 time steps per flapping cycle. The system is time-integrated for three flapping cycles, by which time the aeroelastic response is seen to develop a time-periodic behavior (i.e., the initial transients have decayed due to the presence of $\boldsymbol{C}^*$). Although some techniques exist to prevent the convergence to local (rather than global) topological optima [19], their efficacy for complex multidisciplinary problems requires further research, and are not used here. As such, any of the results given below may not reside at the global optimum. Additionally, finer mesh discretizations are not considered, though the use of a gradient filter should prevent substantially different topologies on finer meshes.

A. Compliant Mechanisms with Fixed Supports

Results are first provided without design of the underlying support structure; only the lower corner of the mechanism box is clamped from moving in either direction, as seen in Fig. 2. As such, the optimization problem [Eq. (25)] only uses the element densities $\boldsymbol{x}$ as design variables. Under this restriction, four optimal compliant mechanism topologies are summarized in Table 5 and Fig. 5. Each of the mechanisms require several hundred iterations of the MMA optimizer to converge, all of the constraints are active (with the exception of $S(\boldsymbol{z})$, which is not included in this section), and all are largely composed of black and white pixels.

The basic topological features of cases 2, 3, and 4 are similar: one member connects the input port (location of the applied vertical actuation force) to a joint below the wing, another travels from this

Table 5 Summary of fixed-support designs

Constraints			Performance				
Case	V^*	u^*	$C_{L,\text{ave}}$	$C_{T,\text{ave}}$	$C_{P,\text{ave}}$	σ_{mech}	σ_{wing}
1	0.17	2 mm	0.0019	0.0178	0.0687	25.85 MPa	18.79 MPa
2	0.235	2 mm	0.0042	0.0977	0.1129	8.68 MPa	27.62 MPa
3	0.3	2 mm	0.0030	0.0735	0.0989	10.45 MPa	24.80 MPa
4	0.3	0.5 mm	0.0025	−0.0028	0.0581	5.78 MPa	14.23 MPa

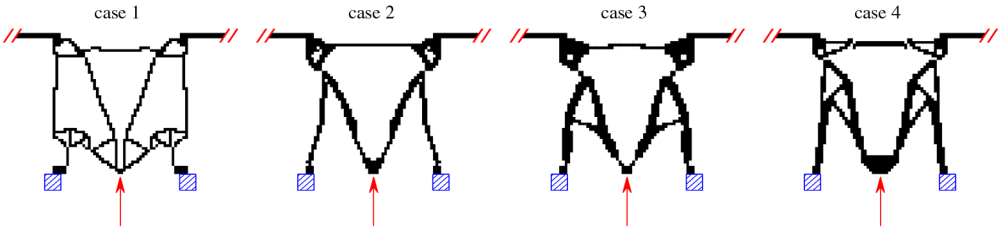

Fig. 5 Optimal topologies of the fixed-support designs: hatched areas are clamped.

joint to the fixed boundary condition (hatched area) at the corner of the mechanism. A positive input force (upwards, as drawn) then creates a negative x-moment about the wing joint (referencing the coordinate system of Fig. 1) and a positive flapping angle (wingtip up). A beamlike member connects the two wings to stabilize the motion. Various combinations of the V^* and u^* constraints add or remove additional members to alter the mechanism mass and/or input deformation for these three cases. Case 1, however, which has a volume fraction of 17%, has a substantially different topology. The resulting motion creates a positive moment about the wing joint: an upwards input force leads to a negative flapping angle (wingtip down), as seen in Fig. 6. This figure also demonstrates the strongly damped response of the flapping structure, indicating the important role of inertial and/or aerodynamic forces in Eq. (15). The flapping angle of case 2, for example, lags the sinusoidal input force by almost 90°. At the instant in time when then deformation is largest ($t/T = 0.5$), the input force is 0.

The lift, thrust, and power coefficients given in Table 5 are defined as:

$$C_L = F_z/(0.5 \cdot \rho_f \cdot U_\infty^2 \cdot c \cdot l) \tag{26}$$

$$C_T = -F_x/(0.5 \cdot \rho_f \cdot U_\infty^2 \cdot c \cdot l) \tag{27}$$

$$C_p = P/(0.5 \cdot \rho_f \cdot U_\infty^3 \cdot c \cdot l) \tag{28}$$

where F_z and F_x are the total aerodynamic forces generated over a single wing [integration of Eqs. (8) and (9)], P is the total power input of the system (discussed below), and the product $c \cdot l$ is the area of that wing. Of the designs given in Table 5, case 2 has the highest cycle-averaged thrust coefficient (over $t/T = 2$ to 3), directly corresponding to its ability to achieve the highest flapping angle (22.8°). The positive lift generated during the downstroke is rotated forward by the angle *atan* $(-\dot{z}/U_\infty)$, and the negative lift during the upstroke is rotated forward by this same angle [26]. If the resulting force in the $-x$ direction is able to overcome the viscous drag of the wing [Eq. (12); induced drag is not modeled here], a net-positive propulsive thrust is produced. Case 4 has a smaller flapping rotation, and is unable to accomplish this: a cycle-averaged negative thrust (i.e., drag) is seen in Table 5. None of the two-dimensional mechanisms in this work can be reasonably expected to produce flapping kinematics different than the general sinusoidal motions seen in Fig. 6, and so the monotonic relationship between high flapping angles and high thrust is a near-constant theme.

It should also be noted that all of the topologies in Fig. 5 make use of "hinges" (two Q4 finite elements connected at a single node). The stresses in these elements are poorly modeled, and many schemes are available to prevent their formation during the optimization process (see, for example, [36]). These tools were found to be less than successful for the current work, as the implicit penalty upon intermediate densities was not strong enough to force a hingeless 0–1 convergence. In any case, postprocessing of each topology needs to be conducted before manufacturing to properly handle hinge areas and other problems [19], though this is not discussed here.

Several snapshots of the flapping motion are given for cases 1 and 3 in Fig. 7, as the input force travels from the downward extreme ($t/T = 1.75$) to the upward extreme ($t/T = 2.25$). As noted above, the two cases are out of phase from each other, with case 1 traveling through a portion of its downstroke, and case 3 through a portion of the upstroke. Most of the local structural deformation for case 1 is seen in the bending of the diagonal members that connect the input port to the wing joint, which bear a compressive load when the input force is positive. Conversely, the cross beam connecting the two wings of case 3 shows the most deformation during the stroke. The aerodynamic loading distribution ($\boldsymbol{F}_{\text{aero}}$) is shown on the right side of each wing, and inertial loads ($\boldsymbol{M} \cdot \ddot{\boldsymbol{u}}$) are shown on the left, scaled by a factor of 3. It should be noted that inertial loads are present within the mechanism portion of the structure as well, but these are not shown.

For these cases, the aerodynamic forces are much larger than the inertial forces, warranting a scaling factor. This is typical of forward flight flapping, though it is speculated that this relationship may swap for smaller hovering wings [37]. Inertial loads are largest at stroke reversal (where acceleration is highest), and aerodynamic loads are largest just beyond the midstroke, where the velocity is highest. Minor aerodynamic forces are seen at stroke reversal as well, directly attributable to the added mass effects used in the model. Both loading patterns are highest at the wingtip, where the wing motion is highest.

The lift and thrust coefficients that result from these flapping motions are given in Fig. 8; only the time-periodic data is given

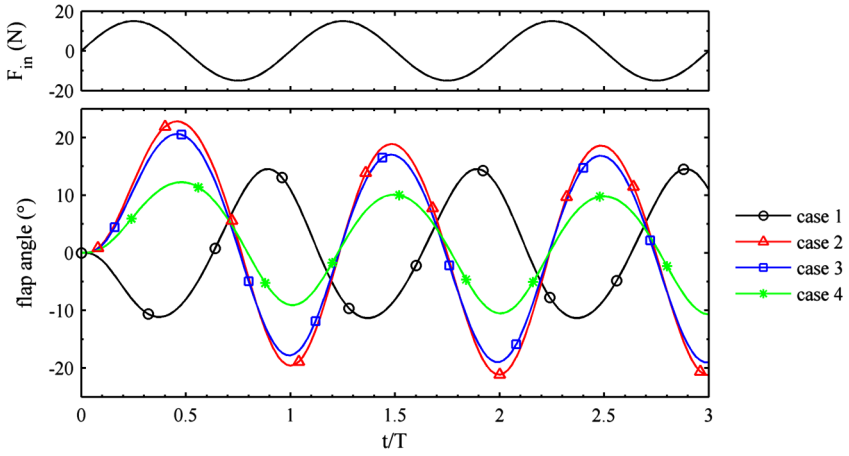

Fig. 6 Time history of flapping rotation for cases 1–4: positive angle corresponds to wingtips up.

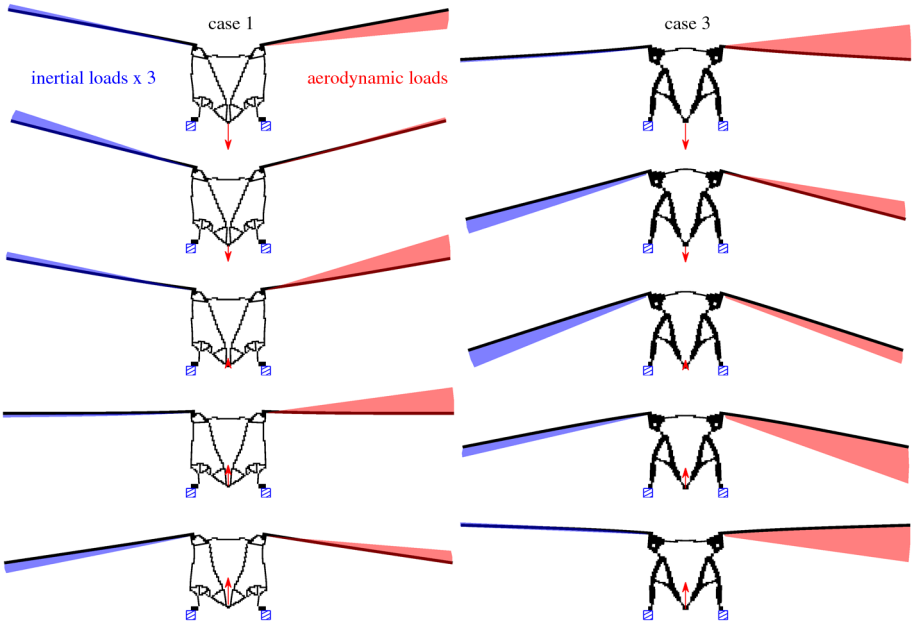

Fig. 7 Five snapshots of the flapping motion between $t/T = 1.75$ and 2.25: case 1 (left), case 3 (right).

(between $t/T = 2$ and 3) as a function of the flapping angle of Fig. 6. The ranking of each cases' force production largely follow the quantitative data of Table 5. Positive lift is produced during the downstroke, negative lift through the upstroke, and the curve is not symmetric, resulting in a nonzero cycle average lift an order of magnitude smaller than the average thrust. This is also an issue with multijointed mechanisms (four-bar linkage, e.g., [38]). An additional equality constraint could be added for lift trim, but is not considered here. It is interesting to note that linear structural modeling would be unable to predict a nonzero average lift, as only a geometrically nonlinear structure registers a difference between a positive and a negative input force. Linear modeling would also inaccurately compute the large deformations seen in Fig. 7 [20].

Positive thrust is produced during both strokes in Fig. 8, with a hysteresis loop produced as a result of the aforementioned flapping asymmetries. At stroke reversal where the velocity is largely zero, a drag force is produced, which is the same for each case: $C_D(0)$. Though not explicitly included in the optimization, power coefficient data is included for completeness in Table 5, and time histories for cases 1 and 3 are given in Fig. 9. The power input P is a sum of the kinetic energy rate (KER $= \dot{\boldsymbol{u}}^T \cdot \boldsymbol{M} \cdot \ddot{\boldsymbol{u}}$), potential energy rate (PER$= \dot{\boldsymbol{u}}^T \cdot \boldsymbol{P}$), and aerodynamic power ($\dot{\boldsymbol{u}}^T \cdot \boldsymbol{F}_{\text{aero}} + \int_0^l U_\infty \cdot \mathrm{d}F_x \cdot \mathrm{d}x$) [8].

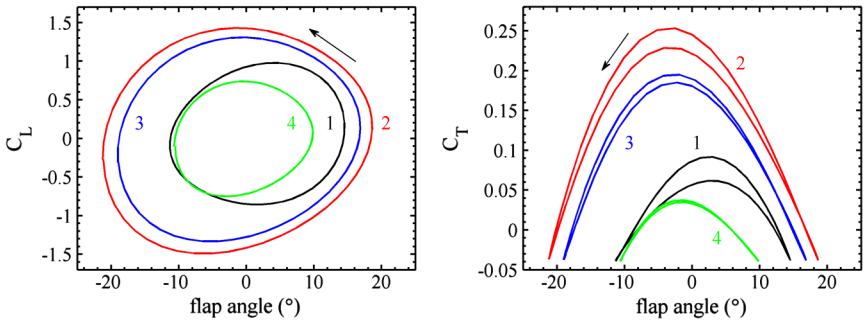

Fig. 8 Time-periodic lift and thrust coefficient orbits for cases 1–4.

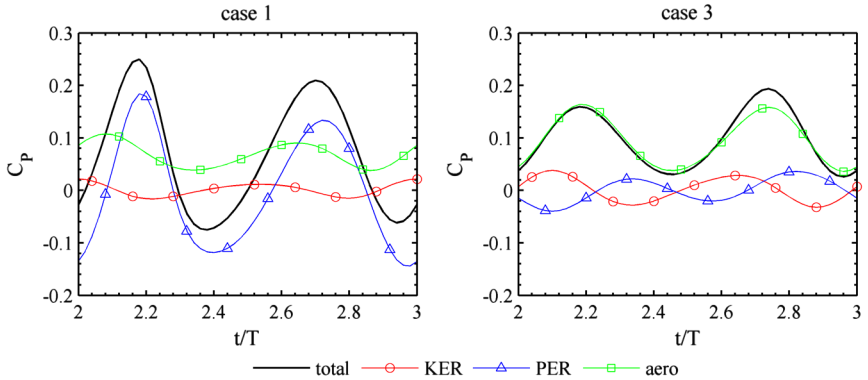

Fig. 9 Breakdown of the power coefficient into components for cases 1 and 3.

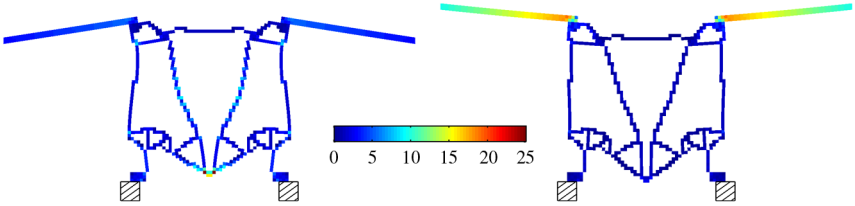

Fig. 10 von Mises stresses (MPa) for case 1: peak mechanism (left) and wing (right) stresses.

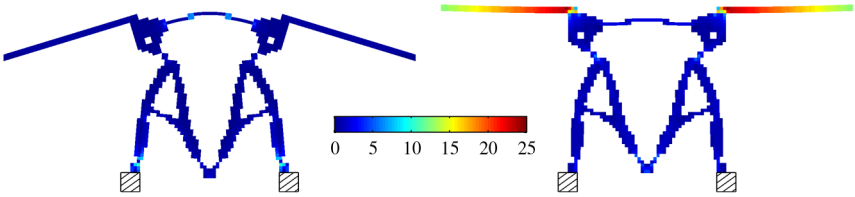

Fig. 11 von Mises stresses (MPa) for case 3: peak mechanism (left) and wing (right) stresses.

Kinetic and potential energy rates are reciprocating processes, but aerodynamic power is always positive: energy is continually expended to push the wings through the fluid. The required power for case 1 is dominated by the potential energy rate expended through internal deformation, though case 3 is dominated by the aerodynamic power related to the broad flapping motions. The potential and kinetic energy rates for case 3 are nearly equal and opposite (reactance cancelation [17]), which will be exactly true for the undamped free-vibration of a structure.

This section concludes with a description of the dynamic stresses generated within the mechanism and the wing. Stresses are not included in the optimization due to difficulties in handling these failure constraints in a gradient-based topology optimization framework, but should certainly be incorporated during postprocessing. Q4 finite elements have well-known accuracy issues with stress computations [27] (particularly within hinge areas [19]), and the mesh is certainly not well-resolved in areas of peak stress, but the following results can still provide insight into potential failure mechanisms. The stress data given in Table 5 indicates the peak von Mises stress seen within the wing spar and the mechanism, at any point in time. Because of the highly coupled nature of the flapping system, no clear trends between stress, V^* and u^* are available. Limiting the input deflection u^* is a well-known surrogate for limiting the mechanism stress [18], and has the desired effect here as well (case 4, though this mechanism is unable to produce thrust).

The von Mises stress field is given in Fig. 10 for case 1 at two instances in time: that which corresponds to the peak mechanism stress and the peak stress in the wing spar. The former is located within the input port via strong shear stresses; the latter is located at the root of the wing. If the wing motion were a pure rigid body rotation these stresses would obviously be zero. Some local bending is observed, however, (clearly seen in Fig. 7), resulting in flexural stresses at the root, linearly decaying to zero at the wingtip (not shown). Similar data is given in Fig. 11 for case 3, where high mechanism stresses are seen in the cross-beam connecting the two wings and the clamped nodes in the corner (though all values are much smaller than for case 1). It should also be noted that a strict comparison of the stress fields of case 1 and 3 should be used with caution: the numerical errors inherent within the hinge singularities are not consistent between the two cases, as the topologies greatly differ.

The yield stress for the ABS plastic used to eventually manufacture the mechanisms is roughly 35 MPa, so all of the stresses in Table 5 are acceptable, notwithstanding a safety factor. This is also true for the wing, where the failure stress of the bidirectional carbon fiber spar would be 80 MPa for matrix cracking (and a much higher threshold would correspond to fiber failure). The stress concentration along the interface of the two materials (seen clearly on the right of Fig. 11) would probably be of greater concern, though a higher level of detail in this area is not available for this conceptual design study. It should also be noted that material fatigue is a substantial consideration in flapping mechanism design [39]; cyclic stresses below yield can still lead to a catastrophic failure. For example, a fatigue life of a million cycles only provides 18 h of flight time (for $\omega=$ 100 rad/s), which is potentially unacceptable. As above, however, the physics governing the fatigue life of brittle ABS plastics are very complicated, and is not considered in this design process. A buckling analysis of the thin members (particularly seen in Case 1) falls into this category as well, an undertaking realistically considered in the postprocessing of each mechanism before fabrication, rather than within the topological optimization process.

B. Compliant Mechanisms with Variable Supports

Results are now provided that consider simultaneous design of the topology and the underlying support structure:, i.e., both element densities $\boldsymbol{x}$ and the support spring coefficients $\boldsymbol{z}$ are design variables. Three optimal compliant mechanisms are summarized in Table 6 and Fig. 12, where the hatched areas indicate a clamped pixel ($z_e = 1$). All remaining pixels correspond to $z_e = z_{\min}$, and thus the support springs have no bearing on the system. As expected, the inclusion of variable supports has a substantial effect upon the optimal topologies. Each design in Fig. 12 places the optimal supports near the wing joint, and is connected to the wing spar by a single-noded hinge. A push rodlike member transmits the load from the input port to a short rocker arm offset from this hinge in the in-board direction (case 5) or the outboard direction (cases 6 and 7). An upwards input

Table 6 Summary of variable-support designs

	Constraints		Performance				
Case	V^*	u^*	$C_{L,\text{ave}}$	$C_{T,\text{ave}}$	$C_{P,\text{ave}}$	σ_{mech}	σ_{wing}
5	0.17	2 mm	0.0015	0.0716	0.0980	11.65 MPa	26.58 MPa
6	0.3	2 mm	0.0028	0.0909	0.1098	14.27 MPa	32.78 MPa
7	0.3	0.5 mm	0.0004	−0.0069	0.0559	4.65 MPa	13.82 MPa

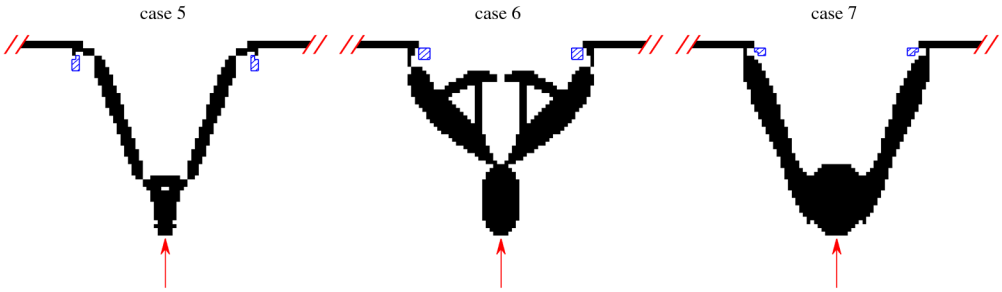

Fig. 12 Optimal topologies of the variable-support designs: hatched areas are clamped.

force induces a negative flapping angle for case 5, and a positive angle for the latter cases.

The ability of the optimizer to easily transmit a rotational moment to the wing via the prudent placement of a support greatly simplifies the design process. The MMA algorithm generally converges in fewer iterations than above (despite the larger number of design variables), each topology is simpler with fewer moving parts, and presumably easier to manufacture (although the logistics of the support structure must now be considered as well). With the exception of case 7 (where the limited input displacement successfully reduces the stress, but is unable to produce a net thrust as with case 4: case 7 may therefore represent a local optima), each design has larger thrust than its constraint-counterpart in Table 5. Case 5 is further able to reduce the peak mechanism stress by 50% from case 1. These general improvements with the introduction of variable supports are consistent with those found in the literature for mechanism design [28].

As above, snapshots of the flapping motion are given for cases 5 and 6 in Fig. 13, as the input force travels from the downward extreme ($t/T = 1.75$) to the upward extreme ($t/T = 2.25$). Both cases (which are out of phase with one another, as discussed) show generally larger aerodynamic and inertial loading than seen in Fig. 7, but have less apparent internal deformation within the mechanism, though the constraint upon the input displacement u^* is always active. Case 6 has a trusslike structure connected to the top of the push rod that connects that input force to the wing joint. These two structures appear to contact one another during a portion of the flapping stroke seen in Fig. 13, but this is only an overlap; contact mechanics are not included in the analysis.

It is not clear what purpose this trusslike structure serves, as it does not bear any stresses (as seen in Fig. 14), and does not appear to contribute to the kinematics. Potentially, this structure appears only to fill out the volume constraint ($V^* = 0.3$) without detrimentally affecting the compliance. The von Mises stresses in Fig. 14 are organized as above, with the instance in time corresponding to peak mechanism stress on the left, and peak wing stress on the right. Peak mechanism stresses for case 6, though below yield (35 MPa) are 36% higher than its fixed-support constraint-counterpart (case 3), though the thrust is 17% higher. This peak stress occurs at the bottom of the downstroke, at the joint between the push rod and the input port.

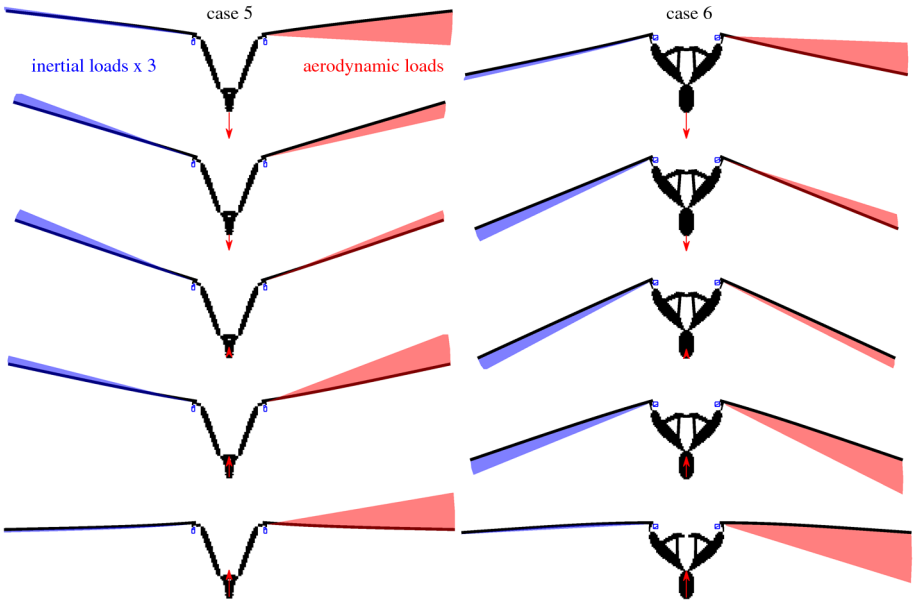

Fig. 13 Five snapshots of the flapping motion between $t/T = 1.75$ and 2.25: case 5 (left), case 6 (right).

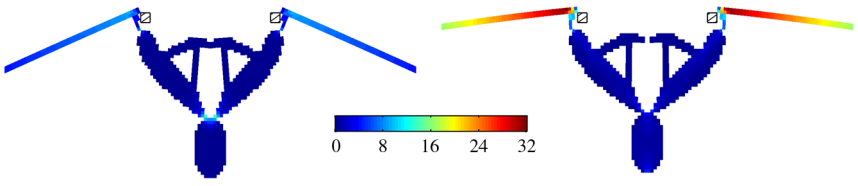

Fig. 14 Von Mises stresses (MPa) for case 6: peak mechanism (left) and wing (right) stresses.

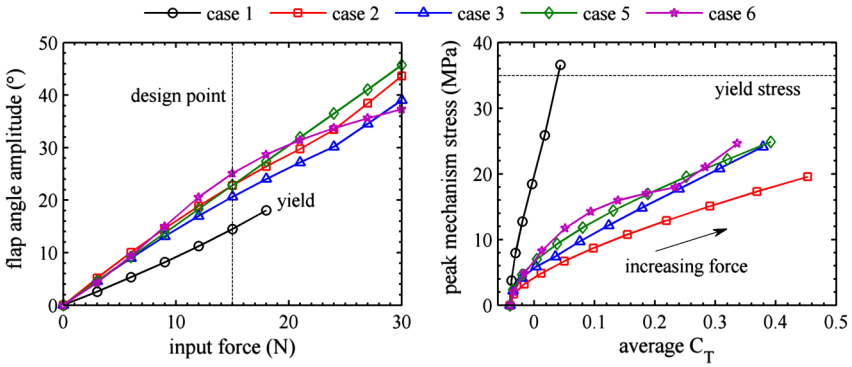

Fig. 15 Flapping performance for increasing actuator input force ($\omega = 100$ rad/s).

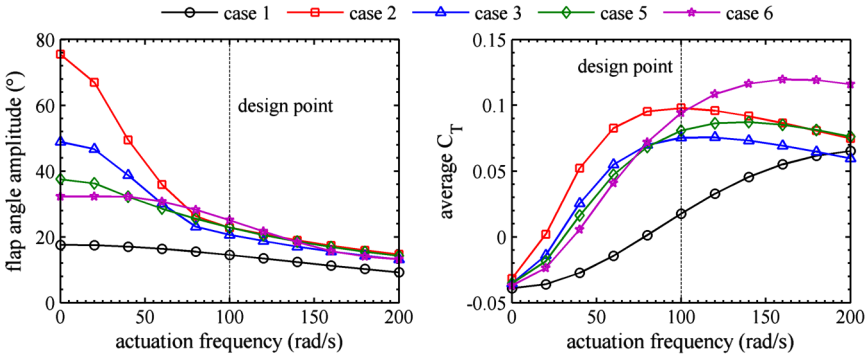

Fig. 16 Flapping performance for increasing actuator input frequency ($f = 15$ N).

Peak wing stress occurs at the root of the rod through the midstroke, and is the largest stress (32 MPa, Table 6) registered for any of the cases studied here. The stresses surrounding the wing-support hinge are relatively large as well; though, as discussed, poorly modeled by the Q4 elements [36].

C. Off-Design Aeroelastic Behavior

Having discussed the physics of the optimal topologies at their design points, attention is turned to the performance of the mechanisms through a range of off-design actuation; namely, the input force magnitude f and frequency ω. Cases 4 and 7 are omitted from this discussion, as their lower input constraints ($u^* = 0.5$ mm) preclude substantial deformations. Furthermore, the important physics of these two cases are similar (though scaled down) to certain topologies considered here. For a fixed actuation frequency, the input force magnitude is varied from 0 to 30 N in Fig. 15. The amplitude of the resulting flapping angle is given on the left, with the design point of 15 N specified. A monolithic relationship exists between the force and flapping rotation, with geometric nonlinearities and/or aerodynamic damping hardening the response under higher input forces.

The right side of Fig. 15 plots the peak von Mises stress within the mechanism as a function of the cycle-averaged thrust coefficient. Each trend of this plot starts with zero input actuation, and so the only force present along the fixed flat-plate wing at 0° angle of attack is the viscous drag. As such, each case starts with a thrust coefficient of -0.04, which is the specified $C_D(0)$ from Table 3. The flapping motion initiates a thrust force, as described above, which counteracts this drag. Each case is able to produce a net-positive thrust within 9 N of input force (which corresponds to a flapping amplitude of about 15°, as seen on the left of Fig. 15), except for case 1. Incidentally, the ABS plastic of case 1 yields at approximately 18 N of input load, but the remaining cases are safely below the yield stress through 30 N (though fatigue, as noted above, may still be an issue, and of course none of the finite element results are adequately mesh-converged about the stress singularities). The location of peak stress in case 6 switches at 24 N, moving from the concentration seen in Fig. 14 to just below the wing joint. From the vantage point of Fig. 15, case 2 is clearly superior to the remaining designs in that it provides the highest level of propulsion with the lowest mechanism stresses, which should translate to a long fatigue life.

Instead of changing the input actuation (which is akin to changing the Strouhal number of the flapping), Fig. 16 fixes the input actuation at 15 N, and traces the response as a function of the actuation frequency. As this frequency approaches zero, the motion is quasi-steady and only the input and elastic forces contribute. The resulting deformation is large and nonlinear, with case 2 in particular flapping at an amplitude of 75°. For nonzero frequencies, the aerodynamic forces resist the motion (as seen in Figs. 7 and 13), and the inertial wing loads require a greater power input (Fig. 9). The net result is a decreased effectiveness of the compliant mechanism with the introduction of aerodynamic and inertial loads, as has been noted experimentally as well.[§] At 200 rad/s, the loads are sufficiently high to limit the flapping amplitude to 15° for most cases.

The thrust data of Fig. 16 begins at $C_D(0)$ for the same reasons as above, and sees an initial quadratic growth with frequency. This growth is diminished, and eventually reversed, by the loss of flapping amplitude noted on the left of Fig. 16. It should be noted that this is strictly a coupled aeroelastic phenomena which has also been observed experimentally [38]; increasing the actuation frequency in a vacuum would see a quadratic growth in thrust, eventually curbed by excessive geometric nonlinearities or inertial loads. From the vantage point of Fig. 16, case 6 is superior, able to achieve a high peak thrust in the high-frequency domain (though case 2 is the best at lower frequencies). The stresses of case 6, which are not shown, are relatively low as well, roughly 10 MPa at the highest frequency. Both effects are thought to be due to the rigid bodylike motions emulated by this variable support topology, which is less susceptible to aerodynamic resistance and elastic failure.

VI. Conclusions

The inclusion of geometrically nonlinear elastic forces, unsteady inertial forces, quasi-steady aerodynamic forces, and oscillating actuation forces into a gradient-based topology optimization scheme

[§]Personal communication with D. Doman [2010].

has been discussed, specifically for compliant flapping wing mechanisms in forward flight. The aeroelastic system is discretized with a monolithic planar finite element grid incorporating both the mechanism and the wing structure, and the nonlinear dynamics are solved with a Newmark scheme and Newton–Raphson subiterations. Design gradients of both the mechanism topology and the underlying support structure are computed analytically, with a direct method.

Several optimization cases are presented; it is generally possible to obtain a topology that can provide the requisite thrust-generating motion, but modifying the constraint boundaries and/or the support details provides greater control over the stresses that develop within the compliant mechanism. This is an important consideration from a fatigue standpoint, where cyclic high-speed stresses can greatly reduce the expected life and reliability of a flapping micro air vehicle. Variable-supports, in particular, are effectively used by the optimizer to create very simple designs with few moving parts, which emulate rigid body motions and limit the stresses which develop throughout the structure.

Acknowledgments

This work is sponsored by the U.S. Air Force Office of Scientific Research under Laboratory Tasks 09RB01COR (monitored by Doug Smith) and 03VA01COR (monitored by Fariba Fahroo). The research was performed while the first author held a National Research Council Associateship Award at the U.S. Air Force Research Laboratory.

References

[1] Ho, S., Nassef, H., Pornsinsirirak, N., Tai, Y., and Ho, C., "Unsteady Aerodynamics and Flow Control for Flapping Wing Flyers," *Progress in Aerospace Sciences*, Vol. 39, No. 8, 2003, pp. 635–681. doi:10.1016/j.paerosci.2003.04.001

[2] Shyy, W., Lian, Y., Tang, J., Liu, H., Trizila, P., Stanford, B., Bernal, L., Cesnik, C., Friedman, P., and Ifju, P., "Computational Aerodynamics of Low Reynolds Number Plunging, Pitching and Flexible Wings for MAV Applications," *Acta Mechanica Sinica*, Vol. 24, No. 4, 2008, pp. 351–373. doi:10.1007/s10409-008-0164-z

[3] Shyy, W., Aono, H., Chimakurthi, S., Trizila, P., Kang, C., Cesnik, C., and Liu, H., "Recent Progress in Flapping Wing Aerodynamics and Aeroelasticity," *Progress in Aerospace Sciences*, Vol. 46, No. 7, 2010, pp. 284–327.

[4] Isogai, K., and Harino, Y., "Optimum Aeroelastic Design of a Flapping Wing," *Journal of Aircraft*, Vol. 44, No. 6, 2007, pp. 2040–2048. doi:10.2514/1.27142

[5] Berman, G., and Wang, Z., "Energy-Minimizing Kinematics in Hovering Insect Flight," *Journal of Fluid Mechanics*, Vol. 582, 2007, pp. 153–168. doi:10.1017/S0022112007006209

[6] Soueid, H., Guglielmini, L., Airiau, C., and Bottaro, A., "Optimization of the Motion of a Flapping Airfoil Using Sensitivity Functions," *Computers and Fluids*, Vol. 38, No. 4, 2009, pp. 861–874. doi:10.1016/j.compfluid.2008.09.012

[7] Stanford, B., and Beran, P., "Analytical Sensitivity Analysis of an Unsteady Vortex Lattice Method for Flapping Wing Optimization," *Journal of Aircraft*, Vol. 47, No. 2, 2010, pp. 647–662. doi:10.2514/1.46259

[8] Stanford, B., Kurdi, M., Beran, P., and McClung, A., "Shape, Structure, and Kinematic Parameterization of a Power-Optimal Hovering Wing," *AIAA Structures, Structural Dynamics, and Materials Meeting*, AIAA 2010-2963, April 2010.

[9] Anderson, M., and Cobb, R., "Frequency Response of a Micro Air Vehicle Flapping Mechanism to Non-Harmonic Forcing," *AIAA Structures, Structural Dynamics, and Materials Meeting*, AIAA Paper No. 2010-2708, April 2010.

[10] Bejgerowski, W., Ananthanarayanan, A., Mueller, D., and Gupta, S., "Integrated Product and Process Design for a Flapping Wing Drive Mechanism," *Journal of Mechanical Design*, Vol. 131, No. 6, 2009, pp. 061006–061015. doi:10.1115/1.3116258

[11] Fenelon, M., and Furukawa, T., "Design of an Active Flapping Wing Mechanism and a Micro Aerial Vehicle Using a Rotary Actuator," *Mechanism and machine theory*, Vol. 45, No. 2, 2010, pp. 137–146. doi:10.1016/j.mechmachtheory.2009.01.007

[12] Maute, K., and Allen, M., "Conceptual Design of Aeroelastic Structures by Topology Optimization," *Structural and Multidisciplinary Optimization*, Vol. 27, No. 1, 2004, pp. 27–42. doi:10.1007/s00158-003-0362-z

[13] Stanford, B., and Ifju, P., "Aeroelastic Topology Optimization of Membrane Structures for Micro Air Vehicles," *Structural and Multidisciplinary Optimization*, Vol. 38, No. 3, 2008, pp. 301–316. doi:10.1007/s00158-008-0292-x

[14] Khatait, J., Mukherjee, S., and Seth, B., "Compliant Design for Flapping Mechanism: a Minimum Torque Approach," *Mechanism and Machine Theory*, Vol. 41, No. 1, 2006, pp. 3–16. doi:10.1016/j.mechmachtheory.2005.06.002

[15] Bolsman, C., Goosen, J., and van Keulen, F., "Design Overview of a Resonant Wing Actuation Mechanism for Application in Flapping Wing MAVs," *International Journal of Micro Air Vehicles*, Vol. 1, No. 4, 2009, pp. 263–272. doi:10.1260/175682909790291500

[16] Madangopal, R., Khan, Z., and Agrawal, S., "Biologically Inspired Design of Small Flapping Wing Air Vehicles Using Four-Bar Mechanisms and Quasi-Steady Aerodynamics," *Journal of Mechanical Design*, Vol. 127, No. 4, 2005, pp. 809–816. doi:10.1115/1.1899690

[17] Tantanawat, T., and Kota, S., "Design of Compliant Mechanisms for Minimizing Input Power in Dynamic Applications," *Journal of Mechanical Design*, Vol. 129, No. 10, 2007, pp. 1064–1075. doi:10.1115/1.2756086

[18] Sigmund, O., "On the Design of Compliant Mechanisms Using Topology Optimization," *Mechanics Based Design of Structures and Machines*, Vol. 25, No. 4, 1997, pp. 493–524. doi:10.1080/08905459708945415

[19] Bendsøe, M., and Sigmund, O., *Topology Optimization*, Springer, Berlin, 2003.

[20] Pederson, C., Buhl, T., and Sigmund, O., "Topology Synthesis of Large-Displacement Compliant Mechanisms," *International Journal of Numerical Methods in Engineering*, Vol. 50, No. 12, 2001, pp. 2683–2705. doi:10.1002/nme.148

[21] Bruns, T., and Tortorelli, D., "Topology Optimization of Non-Linear Elastic Structures and Compliant Mechanisms," *Computer Methods in Applied Mechanics and Engineering*, Vol. 190, No. 26, 2001, pp. 3443–3459. doi:10.1016/S0045-7825(00)00278-4

[22] Min, S., Kikuchi, N., Park, Y., Kim, S., and Chang, S., "Optimal Topology Design of Structures Under Dynamic Loads," *Structural and Multidisciplinary Optimization*, Vol. 17, No. 2, 1999, pp. 208–218. doi:10.1007/s001580050052

[23] Tcherniak, D., "Topology Optimization of Resonating Structures Using SIMP Method," *International Journal of Numerical Methods in Engineering*, Vol. 54, No. 11, 2002, pp. 1605–1622. doi:10.1002/nme.484

[24] Maute, K., and Reich, G., "Integrated Multidisciplinary Topology Optimization Approach to Adaptive Wing Design," *Journal of Aircraft*, Vol. 43, No. 1, 2006, pp. 253–263. doi:10.2514/1.12802

[25] Hsu, C., Evans, J., Vytla, S., and Huang, P., "Development of Flapping Wing Micro Air Vehicles: Design, CFD, Experiment and Actual Flight," *AIAA Aerospace Sciences Meeting*, AIAA2010-1018, Jan. 2010.

[26] Platzer, M., Jones, K., Young, J., and Lai, J., "Flapping Wing Aerodynamics: Progress and Challenges," *AIAA Journal*, Vol. 46, No. 9, 2008, pp. 2136–2149. doi:10.2514/1.29263

[27] Zienkiewicz, O., *The Finite Element Method*, McGraw–Hill, New York, 1972.

[28] Buhl, T., "Simultaneous Topology Optimization of Structure and Supports," *Structural and Multidisciplinary Optimization*, Vol. 23, No. 5, 2002, pp. 336–346. doi:10.1007/s00158-002-0194-2

[29] Hall, J., "Problems Encountered from the Use (or Misuse) of Rayleigh Damping," *Earthquake Engineering and Structural Dynamics*, Vol. 35, No. 5, 2006, pp. 525–545. doi:10.1002/eqe.541

[30] Haftka, R., and Gürdal, Z., *Elements of Structural Optimization*, Kluwer Academic Publishers, Dordrecht, The Netherlands, 1992.

[31] Kim, N., and Choi, K., "Design Sensitivity Analysis and Optimization of Nonlinear Transient Dynamics," *Mechanics of Structures and Machines*, Vol. 29, No. 3, 2001, pp. 351–371. doi:10.1081/SME-100105655

[32] Trier, S., Marthinsen, A., and Sivertsen, O., "Design Sensitivities by the Adjoint Variable Method in Nonlinear Structural Dynamics," *SIMS Simulation Conference*, Scandinavian Simulation Society, Trondheim, Norway, June 1996, pp. 201–212.

[33] Stanford, B., Beran, P., and Kurdi, M., "Adjoint Sensitivities of Time-Periodic Nonlinear Structural Dynamics via Model Reduction," *Computers and Structures*, Vol. 88, No. 19, 2010, pp. 1110–1123. doi:10.1016/j.compstruc.2010.06.012

[34] Stanford, B., and Beran, P., "Formulation of Analytical Design Derivatives for Nonlinear Unsteady Aeroelasticity," *AIAA Structures, Structural Dynamics, and Materials Meeting*, AIAA2010-2999, April 2010.

[35] Svanberg, K., "The Method of Moving Asymptotes: A New Method for Structural Optimization," *International Journal for Numerical Methods in Engineering*, Vol. 24, No. 2, 1987, pp. 359–373. doi:10.1002/nme.1620240207

[36] Poulsen, T., "A Simple Scheme to Prevent Checkerboard Patterns and One-Node Connected Hinges in Topology Optimization," *Structural and Multidisciplinary Optimization*, Vol. 24, No. 5, 2002, pp. 396–399. doi:10.1007/s00158-002-0251-x

[37] Combes, S., and Daniel, T., "Into Thin Air: Contributions of Aerodynamic and Inertial-Elastic Forces to Wing Bending in the Hawkmoth Manduca Sexta," *Journal of Experimental Biology*, Vol. 206, No. 17, 2003, pp. 2999–3006. doi:10.1242/jeb.00502

[38] Wu, P., Stanford, B., and Ifju, P., "Flapping Wing Structural Deformation and Thrust Correlation Study with Flexible Membrane Wings," *AIAA Journal*, Vol. 48, No. 9, 2010, pp. 2111–2122. doi:10.2514/1.J050310

[39] Yan, J., Wood, R., Avadhanula, S., Sitti, M., and Fearing, R., "Towards Flapping Wing Control for a Micromechanical Flying Insect," *IEEE International Conference on Robotics and Automation*, IEEE Publications, Piscataway, NJ, May 2001.

R. Kapania
Associate Editor